Journal of Luminescence 236 (2021) 118075

Contents lists available at ScienceDirect

Journal of Luminescence

journal homepage: http://www.elsevier.com/locate/jlumin

Fully nonlinear photocarrier radiometry / modulated photoluminescence dynamics in semiconductors: Theory and applications to quantitative deconvolution of multiplexed photocarrier density wave interference and recombination processes

Qiming Sun [a,b], Alexander Melnikov [b], Andreas Mandelis [a,b,*], Yaqin Song [b,c]

[a] School of Optoelectronic Science and Engineering, University of Electronic Science and Technology of China, Chengdu, 610054, China
[b] Center for Advanced Diffusion-Wave and Photoacoustic Technologies, University of Toronto, Toronto, M5S 3G8, Canada
[c] School of Aerospace, Xi'an Jiaotong University, Xi'an, 710049, China

ARTICLE INFO

Keywords:
Modulated photoluminescence
Photocarrier radiometry
Lifetime metrology
Nonlinear dynamics
Physical lifetime resolution
Homodyne and heterodyne detection

ABSTRACT

Semiconductor characterization techniques based on modulated photoluminescence (PL) combine the general advantages of PL metrology with the superior quality benefits of modulated signal generation and lock-in detection. The exciting field of camera-based PL imaging has recently emerged and is proving to be very promising for in-line spatially resolved and globally integrated monitoring of dynamic electronic properties of semiconductor materials and devices during various fabrication and manufacturing stages. Yet, the multiple nonlinearities involved in dynamic PL and their behavior under modulated excitation have neither been adequately addressed theoretically nor quantitatively analyzed, resulting in either misleading interpretations of experimental data or leading to the popular compromise of using the physically ambiguous concept — effective lifetime — as the target measurement parameter, which lumps all the excess carrier de-excitation events together and creates persistent confusion in the comparison among different lifetime measurement techniques. By taking three dominant nonlinearities into account that contribute to dynamic PL responses in Si, the present investigation provides a fully nonlinear frequency-domain model of carrier recombination dynamics under harmonically modulated excitation, based on which six intrinsic electronic parameters of a Si wafer can be resolved and measured simultaneously, i.e. the doping density, the two Shockley-Read-Hall time constants, the radiative recombination coefficient, and the two Auger recombination coefficients. The combined theoretical and experimental technique represents a time demultiplexing methodology which allows the deconvolution of temporally superposed excess carrier de-excitation processes which might otherwise remain unresolved — hidden in superposition — as is typically the case with conventional effective lifetime metrologies. This all-optical and noncontacting electronic quality control approach links substrate property optimization and key device-fabrication processing steps to optimized device performance through elucidating the relationship between the global behavior of the system/device/material and the specific controlling/limiting dynamic (opto)electronic process (es) behind it.

1. Introduction

In the modern IC and photovoltaics industry, carrier recombination and transport parameters such as lifetimes and diffusion lengths are routinely measured. While solar cell efficiency is directly related to photocarrier lifetimes [1], the latter play a less direct role in the performance of micro- and nano-electronic IC devices, yet lifetime measurement techniques are still universally adopted as process cleanliness monitoring at almost all stages of research, fabrication, and manufacturing. This is so because defect densities as low as sub-ppb levels in semiconductors can be easily detected via simple room-temperature lifetime measurements [2,3].

Lifetime characterization techniques based on modulated photoluminescence (MPL) [4,5] and photocarrier radiometry (PCR) [6]

* Corresponding author. School of Optoelectronic Science and Engineering, University of Electronic Science and Technology of China, Chengdu, 610054, China.
E-mail address: mandelis@mie.utoronto.ca (A. Mandelis).

https://doi.org/10.1016/j.jlumin.2021.118075
Received 5 October 2020; Received in revised form 19 March 2021; Accepted 22 March 2021
Available online 26 March 2021

combine the general advantages of PL-based methods, such as all-optical detection and defect sensitivity, with the benefits of lock-in detection which includes superior signal-to-noise ratio (SNR) and stand-alone quantitative (calibration free) capability via phase-sensitive analysis in the frequency domain [5–7]. In the past two decades, PCR emerged as the result of re-casting the PL effect in terms of photocarrier density non-equilibrium thermodynamics which encompasses radiative and non-radiative recombination processes in the limit of non-equilibrium photocarrier rate process kinetics. PCR designation has thus been specifically associated with the purely intrinsic radiative emission component of the photocarrier de-excitation physics [6] to the exclusion of other recombination processes that contribute indirectly to the overall PL emission dynamics. Those indirect contributions are largely associated with Shockley-Read-Hall (SRH) [8,9] and Auger [10,11] recombination processes. Along with direct radiative recombination, they collectively constitute the phenomenon of PL photon emissions in semiconductors. In the present investigation in which strongly nonlinear processes mix photocarrier de-excitation pathways involving all aforementioned recombination processes, the notation PCR/MPL will be adopted throughout to indicate detection modalities involving the entirety of physical effects giving rise to infrared photon emission processes originating in purely radiative, SRH and Auger recombinations, as opposed to non-radiative recombinations which are detected by the PCR-complementary modality of semiconductor photothermal radiometry (PTR) [12]. Furthermore, the dynamic imaging term "lock-in carrierography" (LIC) [13] and its homodyne and heterodyne derivative modalities are direct extensions of PCR. Those definitions will be retained in this report.

Modulation-frequency-scanned PCR [6] has been shown to be capable of quantitatively characterizing bulk, surface, interface, junction, and trap-state properties of a wide range of semiconductor materials and devices [14–18]. Furthermore, with the development of modern near-infrared (NIR) cameras, the exciting advent of camera-based PL imaging [5,19,20], including the introduction of LIC [13], has emerged as a promising diagnostic field for fast spatially-resolved and globally-integrated quantitative characterization of large wafers and solar cells [21–28]. Despite the long-term development and the broad applications of PCR/MPL, there remains a fundamental problem in the rigorous theoretical description and data processing: although identified early on as part of PCR signal generation [29], the multiple nonlinearities involved in carrier recombination kinetics and how they behave under modulated excitation have not been adequately addressed and quantitatively analyzed [5,30]. For the convenience of theoretical description, PL can be divided into two processes with three key quantities involved: from optical generation $G(t)$ to excess carrier density $n(t)$, and from excess carrier density $n(t)$ to PCR/MPL signal $S(t)$. From the signal generation point of view, neither process is linear: Following the work of Tolev et al. [29] in the past five years the second nonlinear process (from $n(t)$ to $S(t)$) has been studied extensively [30–34] and a rigorous theoretical treatment of this nonlinearity has been established, while the first nonlinear process (from $G(t)$ to $n(t)$) governed by the carrier recombination rate equation still lacks thorough investigation. Classic carrier recombination theories [8,9,35] show that neither intrinsic (radiative and Auger recombination) nor extrinsic recombination processes (electron-hole pair SRH recombination through recombination centers) exhibit linear recombination rates with respect to $n(t)$. In other words, except for limiting cases, the expression $n(t)/\tau$ with a constant recombination lifetime τ is too simplistic to describe actual recombination rates. Much of the PCR/MPL literature to-date has neglected this problem probably due to the complicated nature of the SRH, radiative, and Auger nonlinearities under light intensity modulation [5,6,10,11,30].

A widely adopted way to bypass the nonlinearity physics has been the introduction of an injection-level-dependent effective lifetime $\tau(n)$. This quantity is the target parameter of most lifetime characterization techniques such as microwave photoconductance, surface photovoltage, and PCR/MPL, in steady-state, quasi-steady-state, modulated, or transient modes. In most cases, τ is the quantity that practitioners in the field most often use [3,36]. Despite its popularity and simplicity, it is worth noting the inherent inadequacy in the concept of the effective lifetime: 1) it lacks a rigorous mathematical definition so that different techniques, or the same technique operating under different modalities, may yield order-of-magnitude differing effective lifetimes for the same material or device [5,37–40]; and 2) it is a highly averaged (both spatially and temporally) parameter that lumps together intrinsic and extrinsic recombination, and surface and bulk recombination, thereby having to introduce *a priori* assumptions that making it difficult for scientists and engineers to understand and evaluate physical electronic factor(s) that limit device performance.

The theoretical treatment and the experimental corroboration presented in this work mainly target high quality semiconductor wafer typically used for industrial device fabrication. By taking SRH, radiative, and Auger nonlinearities into account (the three dominant recombination mechanisms in c-Si) [3], the present study provides a frequency-domain nonlinearity analysis of the photocarrier recombination dynamics involved in PCR/MPL. The theory was corroborated by homodyne intensity-scan experimental results, and, instead of a single effective lifetime value, six key electronic parameters of a c-Si wafer, i.e. the doping density, the two SRH time constants [8,9], the radiative recombination coefficient, and the two Auger recombination coefficients, were simultaneously extracted through best fitting the theory to the experimental data. The results yield so-far-lacking physical insights into the performance of materials preparation and their impact on photocarrier dynamic/kinetic processes. Furthermore, the developed fully nonlinear theory provides a more rigorous quantitative description and better understanding of the signal generation mechanisms of LIC imaging in the heterodyne mode, also referred to as heterodyne lock-in carrierography (HeLIC) [13,26,31,41]. HeLIC features the use of two excitation laser beams modulated at two adjacent frequencies with a small difference (beat frequency). By virtue of the inherent PCR/MPL nonlinearity, the nonlinear frequency mixing results in the generation of a signal component at the beat frequency which carries high-frequency information but is slow enough for allowing millisecond to sub-microsecond physical processes to be accessed dynamically through today's state-of-the-art, yet much slower (100-Hz), frame-rate near-infrared (NIR) cameras. A major motivation for the present nonlinear photocarrier transport investigations has been the appearance of an unexpected abnormal HeLIC amplitude suppression ("notch") phenomenon sensitive to excitation intensity and modulation frequency which cannot be explained by previous linear PCR/MPL theories. We observed this phenomenon for a wide range of semiconductor materials in both heterodyne PCR frequency scans and HeLIC images and have been able to quantitatively describe it by means of the present fully nonlinear theory as a destructive interference among CDWs generated from different nonlinearity sources. The notch phenomenon, not observed in regular homodyne modulation modalities but only emerging in heterodyne excitation and detection, helps uniquely identify/deconvolve the various lifetimes, as heterodyne signal generation entirely relies on the nonlinear frequency mixing of target materials, and different sources of nonlinearities impart different levels of contribution to the overall signal, in which the feasibility and sensitive resolution of the overlapping dynamic processes originates. Consistent with the analysis of homodyne PCR and LIC experiments, the application of the developed theory resulted in the measurement of three isolated recombination rates/lifetimes, thereby allowing PCR/MPL to produce spatially and temporally resolved quantitative optoelectronic relaxation parameters in time-multiplexed photocarrier de-excitation manifolds.

2. Theory of PCR/MPL of semiconductors

2.1. General considerations

Although PCR/PL-based techniques measure signals associated with band-to-band carrier radiative recombination-induced photon emissions, other recombination processes such as SRH and Auger recombination also enter the PL signals through their impact on the photocarrier density which, taking Si as an example, is governed by the partial differential ambipolar carrier diffusion equation [2,5] and the associated initial and boundary conditions (assuming optical excitation commences at $t = 0$)

$$\frac{\partial n(x,y,z,t)}{\partial t} = \nabla\cdot[D\nabla n(x,y,z,t)] + G(x,y,z,t) - \sum_i R_i \tag{1a}$$

$$n(x,y,z,0) = 0 \tag{1b}$$

$$D\frac{\partial n(x,y,z,t)}{\partial z}\bigg|_{z=0} = s_f n(x,y,0,t) \tag{1c}$$

$$-D\frac{\partial n(x,y,z,t)}{\partial z}\bigg|_{z=L} = s_b n(x,y,L,t) \tag{1d}$$

where D is the ambipolar diffusion coefficient, R_i is the recombination rate of the ith bulk recombination mechanism, s_f (s_b) is the front (back) surface recombination velocity, and L is the wafer thickness. Equation (1a) is based on the charge neutrality approximation, which holds for relatively slow time scales, so that the drift term with the internal electric field created by excess electron-hole pairs is neglected.

Equation (1a) is fundamental and appears in most semiconductor textbooks. It is essentially a strongly nonlinear partial differential equation, as D, R_i, and s_f (s_b) are all functions of $n(x,y,z,t)$. Specifically, for c-Si, $D = (n + p)D_nD_p/(nD_n + pD_p)$ with values ranging from the ambipolar diffusivity (18 cm^2/s) at high-injection levels to the minority carrier diffusivity (36 or 12 cm^2/s, depending on the doping type) at low-injection levels [42]. As a result, the D value is different at different locations of a wafer under illumination. Furthermore, considering the PCR/MPL case, the photocarrier density is modulated periodically with time, and consequently the D value also oscillates, rendering Eq. (1) very complicated and impossible to solve analytically. Although this study is pursuing a rigorous analysis of the frequency domain behavior of PCR/MPL, the simplification generally adopted in semiconductor carrier lifetime measurements has consistently used the spatially averaged photocarrier density $n(t)$ instead of $n(x,y,z,t)$ [3–5].

However, the limitations of the spatial-averaging approximation must be taken into consideration. In general, thin samples with large diffusivity, long effective lifetime, weak surface recombination, and under low-frequency excitation are ideal for the spatial-averaging approximation, while the opposite will cause discrepancy between theory and experiment, and will eventually limit the measurement precision of the semiconductor parameters. As to how much error will be caused by the spatial-averaging approximation in a specific case, a quantitative analysis and numerical simulations need to be carried out which is outside the scope of this paper. An illuminating investigation regarding this issue can be found in Ref. [5].

Based on the spatial averaging simplification, and confining the analysis within the three dominant recombination processes (SRH, radiative, and Auger), Eq. (1a) is reduced to the carrier generation/recombination rate equation [3].

$$\frac{\mathrm{d}}{\mathrm{d}t}n(t) = G(t) - R_{SRH} - R_{rad} - R_{Auger} \tag{2}$$

where $G(t)$ should now be perceived as the spatially averaged carrier generation rate, and R_{SRH}, R_{rad}, and R_{Auger} denote the rates of SRH, radiative, and Auger recombination, respectively. The latter two mechanisms are inherent for all semiconductors, and they generally occur even for ideal materials without any lattice imperfection and impurities, while SRH recombination is extrinsic, caused by electronic states in the band gap, which manifests itself both as bulk and interface recombination. Therefore, surface recombination should be classified as SRH recombination [3].

All three recombination rates in Eq. (2) are nonlinear with respect to the excess carrier density. Without loss of generality, taking p-type c-Si as example and neglecting the influence of the intrinsic carrier density (which is reasonable for extrinsic semiconductors and for not very high temperatures), the three recombination rates can be written as [3,36].

$$R_{SRH} = \frac{n(n+p_0)}{(\tau_p+\tau_n)n + \tau_n p_0} \tag{3a}$$

$$R_{rad} = Bn(n+p_0) \tag{3b}$$

$$R_{Auger} = C_p(n+p_0)^2 n + C_n(n+p_0)n^2 \tag{3c}$$

where p_0 is the equilibrium majority carrier (hole) density generated by p-type doping and τ_n (τ_p) are the electron (hole) capture time constants at the defect state, respectively. They were introduced by Hall, Shockley, and Read and are related to thermal carrier velocities and carrier capture cross sections [8,9]. B is the radiative recombination coefficient and C_p and C_n are the Auger recombination coefficients (C_p corresponds to the process of the released recombination energy of an electron-hole pair transferring to another free hole, while C_n refers to that transferring to another free electron). The impact of surface recombination on PL signals is through its direct influence on the two SRH time constants τ_n and τ_p in Eq. (3a).

Due to $n = p$ (electrical neutrality), the term $(n + p_0)$ that appears several times in Eq. (3) should be perceived as the total hole density (excess plus equilibrium), while $n + n_0 \approx n$ is the total free electron density, in view of the fact that in p-type c-Si n_0 is much lower than all the other densities ($n_0p_0 \approx 10^{20}$ cm^{-6}; since p_0 is from 10^{14}–10^{17} cm^{-3} for usual doping levels, then n_0 is very small and thus negligible). Based on this understanding, the physical meaning of Eqs. (3b) & (3c) is very clear: the radiative recombination rate should be proportional to the product of the total free electron and hole densities, and this is exactly what Eq. (3b) describes, with B being the proportionality factor. Similarly, the Auger recombination rate (a three-particle-involving process) should be proportional to the product of the total free electron and the total hole densities multiplied by either the total free electron density (the C_n Auger process) or the total hole density (the C_p Auger process).

The SRH formula shown in Eq. (3a) is not as intuitive as the latter two, as it is a phonon-mediated recombination via electronic states within the band gap. It was founded on statistical considerations about carrier capturing of a deep-level defect (also referred to as recombination center, distinguishing itself from shallow defect states often acting as carrier traps [5]) in the bandgap of a non-degenerate semiconductor.

It is instructive to examine two limiting cases of Eq. (3) corresponding to low- and high-injection levels. The units of Eq. (3) are those of a rate [$cm^{-3}s^{-1}$], and it is clear that rate and lifetime are simply related

$$\tau_{SRH} = \frac{n}{R_{SRH}} = \frac{(\tau_p+\tau_n)n + \tau_n p_0}{n+p_0} \tag{4a}$$

$$\tau_{rad} = \frac{n}{R_{rad}} = \frac{1}{B(n+p_0)} \tag{4b}$$

$$\tau_{Auger} = \frac{n}{R_{Auger}} = \frac{1}{C_p(n+p_0)^2 + C_n(n+p_0)n} \tag{4c}$$

It is worth noting that on the lhs of Eq. (4) lie the “common, effective, and varying” lifetimes found in much of the literature, while on the rhs are the inherent parameters of the material under investigation. The

parameters on the rhs are the target parameters to be determined in this work, while those on the lhs are only used in this study for a phenomenological interpretation of specific kinetic processes. For low-level-injection cases where $n << p_0$, Eq. (4) reduce to

$$\tau_{SRH} \xrightarrow{n<<p_0} \tau_n \tag{5a}$$

$$\tau_{rad} \xrightarrow{n<<p_0} \frac{1}{Bp_0} \tag{5b}$$

$$\tau_{Auger} \xrightarrow{n<<p_0} \frac{1}{C_p p_0^2} \tag{5c}$$

which means that in the low-injection limit, all three lifetimes are constant, and consequently Eq. (2) can be simplified to a linear ordinary differential equation, i.e., the excess carrier density is linear with the generation rate

$$\frac{d}{dt}n(t) = G(t) - \frac{n(t)}{\tau},\ n(t) << p_0 \tag{6}$$

where $\tau^{-1} = \tau_n^{-1} + Bp_0 + C_p p_0^2$ is the reciprocal of the effective lifetime which lumps the three separated lifetimes together.

2.2. For high-injection levels where $n \gg p_0$, we obtain

$$\tau_{SRH} \xrightarrow{n>>p_0} \tau_p + \tau_n \tag{7a}$$

$$\tau_{rad} \xrightarrow{n>>p_0} \frac{1}{Bn} \tag{7b}$$

$$\tau_{Auger} \xrightarrow{n>>p_0} \frac{1}{(C_p + C_n)n^2} \equiv \frac{1}{C_a n^2} \tag{7c}$$

where $C_a = C_p + C_n$ is often called the ambipolar Auger coefficient [3]. It is seen from Eq. (7a) that the SRH lifetime is constant again at high injection levels, while the latter two lifetimes become dependent on the excess carrier density, an indication of a nonlinear correlation between the excess carrier density and the recombination rate, and subsequently between the excess carrier density and the generation rate. For intermediate-injection conditions, all three lifetimes are not constant, and therefore the fully nonlinear rate equation must be solved. Substituting Eq. (3) into Eq. (2) yields

$$\frac{dn}{dt} = G - \frac{n(n+p_0)}{(\tau_p + \tau_n)n + \tau_n p_0} - Bn(n+p_0) - C_p(n+p_0)^2 n - C_n(n+p_0)n^2 \tag{8}$$

Equation (8) will be solved and analyzed in what follows. It is worth noting that a similar equation proposed by Guidotti et al. [10].

$$\frac{dn}{dt} = G - \frac{n}{\tau} - Bn^2 - Cn^3 \tag{9}$$

is not rigorous; it holds only under high-injection conditions $n \gg p_0$: by using the limits shown in Eq. (7), Eq. (8) can be simplified to Eq. (9).

2.3. Frequency-domain theory of homodyne PCR/MPL

PCR/MPL in the homodyne mode uses a harmonically modulated laser to excite electronic materials, which is in fact the conventional form of PCR/MPL [5,6]. The term "homodyne" is added here in order to distinguish itself from the newly developed HeLIC imaging modality where two modulated lasers with a fixed frequency difference are used [13,26,31]. For the case of homodyne excitation, laser power is modulated around a mean value. Conventionally, the laser power is fully modulated from 0 to a maximum. Recently, a "ripple" excitation mode featuring small modulation depth compared to the dc level was introduced to bypass the complicated "modulated lifetime" problem, so as to simplify theoretical interpretation and guarantee measurement self-consistency [30]. Although in this study the "modulated lifetime" will be rigorously investigated without relying on the ripple mode to bypass this problem, the ripple mode excitation was also implemented in our experiments along with the full modulation excitation in order to acquire more experimental information and deeper understanding of the effects of nonlinearities.

The generation rate in the homodyne mode can be written as

$$\begin{cases} G(t) = G_0(1 + \gamma\cos\omega t) = G_0\left(1 + \frac{1}{2}\gamma e^{i\omega t} + \frac{1}{2}\gamma e^{-i\omega t}\right) \\ G_0 \equiv \frac{I_0(1-R)}{h\nu L} \end{cases} \tag{10}$$

Here, I_0 is the average laser intensity, R is the optical reflectivity of the wafer surface against the excitation laser, $h\nu$ is the incident photon energy, $\omega = 2\pi f$ is the angular modulation frequency, and γ is the amplitude modulation depth factor ranging from 0 to 1 ($\gamma = 1$ is the conventional full modulation and $\gamma = 0$ means pure dc excitation).

For simplicity, complex notation is adopted in Eq. (10) and will be maintained henceforth. It is seen that for $\gamma = 1$, the amplitude of the ω component in complex notation is half that of the dc component, due to the existence of the negative frequency counterpart. In cases of nonlinear problems, it is indispensable to write out all the negative frequency terms.

To solve Eq. (8) with the generation rate defined by Eq. (10), one can first reshape Eq. (8) into the standard multinomial form through multiplying each term in Eq. (8) by the denominator of the SRH recombination term, which yields

$$\left[(\tau_p + \tau_n)n + \tau_n p_0\right]\frac{dn}{dt} = \left[(\tau_p + \tau_n)n + \tau_n p_0\right]G - A_1 n - A_2 n^2 - A_3 n^3 - A_4 n^4 \tag{11}$$

with

$$A_1 = (1 + Bp_0\tau_n + C_p p_0^2 \tau_n)p_0 \tag{12a}$$

$$A_2 = 1 + Bp_0(\tau_p + 2\tau_n) + C_p p_0^2(\tau_p + 3\tau_n) + C_n p_0^2 \tau_n \tag{12b}$$

$$A_3 = B(\tau_p + \tau_n) + C_n p_0(\tau_p + 2\tau_n) + C_p p_0(2\tau_p + 3\tau_n) \tag{12c}$$

$$A_4 = (C_p + C_n)(\tau_p + \tau_n) \tag{12d}$$

Due to the nonlinear nature of Eq. (11), infinitely many frequency components of the carrier density waves will be generated through nonlinear mixing processes even under single-frequency excitation expressed by Eq. (10). As a result, one can assume the solution of Eq. (11) in the frequency-domain to be in the form of a complex Fourier series

$$n(t) = \sum_{k=-\infty}^{+\infty} n_k e^{ik\omega t} \tag{13}$$

where n_k is the complex amplitude of the kth harmonic. In the theory of complex Fourier expansion of a real function (optical modulation signal is a real function, and so as the carrier density), the negative frequency term is the complex conjugate of the positive counterpart, which means that their amplitudes are the same and their phases have the opposite signs.

Inserting Equation (13) into Eq. (11) and writing explicitly the time-derivative term results in the following multi-frequency equation

$$\left(\sum_{k=-\infty}^{+\infty} \mathrm{i}k\omega n_k \mathrm{e}^{\mathrm{i}k\omega t}\right)\left((\tau_\mathrm{p}+\tau_\mathrm{n})\sum_{k=-\infty}^{+\infty} n_k \mathrm{e}^{\mathrm{i}k\omega t}+\tau_\mathrm{n}p_0\right)=\left(\sum_{k=-1}^{+1} G_k \mathrm{e}^{\mathrm{i}k\omega t}\right)\left((\tau_\mathrm{p}+\tau_\mathrm{n})\sum_{k=-\infty}^{+\infty} n_k \mathrm{e}^{\mathrm{i}k\omega t}+\tau_\mathrm{n}p_0\right)-A_1\sum_{k=-\infty}^{+\infty} n_k \mathrm{e}^{\mathrm{i}k\omega t}$$
$$-A_2\left(\sum_{k=-\infty}^{+\infty} n_k \mathrm{e}^{\mathrm{i}k\omega t}\right)^2-A_3\left(\sum_{k=-\infty}^{+\infty} n_k \mathrm{e}^{\mathrm{i}k\omega t}\right)^3-A_4\left(\sum_{k=-\infty}^{+\infty} n_k \mathrm{e}^{\mathrm{i}k\omega t}\right)^4 \tag{14}$$

where, for the summation representation of $G(t)$, there are only three terms for the homodyne case, as shown in Eq. (10). Each frequency component in Eq. (14) must be balanced on both sides of the equal sign. The contributions of the linear, square, cubic, and quartic terms to the $\mathrm{e}^{\mathrm{i}k\omega t}$ components of Eq. (14) are

$$\mathrm{e}^{\mathrm{i}k\omega t}:\begin{cases} A_1 n_k \\ A_2\sum_{m=-\infty}^{+\infty} n_m n_{k-m} \\ A_3\sum_{m=-\infty}^{+\infty}\sum_{l=-\infty}^{+\infty} n_m n_l n_{k-m-l} \\ A_4\sum_{m=-\infty}^{+\infty}\sum_{l=-\infty}^{+\infty}\sum_{j=-\infty}^{+\infty} n_m n_l n_j n_{k-m-l-j} \end{cases} \tag{15}$$

The product of $\mathrm{d}n/\mathrm{d}t$ and $n(t)$, and the product of $G(t)$ and $n(t)$ appearing in Eq. (14) can be treated in the same manner as that of the square term in Eq. (15).

Expressions (15) are essentially in the form of convolution: on treating the square term as the product of two functions, the convolution theorem states that the Fourier transform of the product of two functions in the time domain is equal to the convolution of their frequency spectra.

Based on the above analysis, the $\mathrm{e}^{\mathrm{i}k\omega t}$ component of Eq. (14) can be written as

$$0=(G_k-\mathrm{i}k\omega n_k)\left[\tau_\mathrm{n}p_0+(\tau_\mathrm{p}+\tau_\mathrm{n})\sum_{m=-\infty}^{+\infty} n_{k-m}\right]-A_1 n_k-A_2\sum_{m=-\infty}^{+\infty} n_m n_{k-m}$$
$$-A_3\sum_{m=-\infty}^{+\infty}\sum_{l=-\infty}^{+\infty} n_m n_l n_{k-m-l}-A_4\sum_{m=-\infty}^{+\infty}\sum_{l=-\infty}^{+\infty}\sum_{j=-\infty}^{+\infty} n_m n_l n_j n_{k-m-l-j} \tag{16}$$

where $G_k = 0$ for $|k| > 1$.

From Eq. (16) one can see that not only n_k, but also the CDW complex amplitudes at all other frequency components, enter the $\mathrm{e}^{\mathrm{i}k\omega t}$ component-associated algebraic equation which is a consequence of nonlinearity-induced coupling among different frequency components. Therefore, to obtain a sufficiently accurate expression for a CDW complex amplitude n_k, one must solve the infinite system of coupled algebraic equation (16) for all k, with the highest power being four.

In practice, the infinite system of equations must be truncated. Since for homodyne excitation the generation rate $G(t)$, acting as the driving force of the system of equations, only has the dc and the fundamental frequency components, the strength of higher harmonics decays rapidly with respect to k. As to how fast it decays, it will depend on specific parameters chosen in the calculation. Assuming a truncated order k_max corresponds to an acceptable numerical tolerance, the infinite system of equations is reduced to $2k_\mathrm{max}+1$ (from $-k_\mathrm{max}$ to k_max). Recall that n_{-k} is the complex conjugate of n_k, so actually one only needs to simultaneously solve $k_\mathrm{max}+1$ complex-valued equations numerically. The error caused by a certain truncated order depends on the specific electronic parameters, the excitation intensity, and the modulation frequency.

It can be seen from Fig. 1 that besides the dc and the fundamental components, higher harmonics exist, due to the nonlinear nature of Eq. (16). Frequency components other than integer multiples of the fundamental frequency have, and should have, zero amplitude, as they don't exist in the spectrum of $n(t)$. The 10th harmonic has an amplitude four-orders-of-magnitude lower than that of the dc component at 100 Hz (Fig. 1b), and even much lower at 1 kHz, Fig. 1c, which is already below the numerical noise level. The fact that the amplitude of carrier density waves decreases at high modulation frequencies is clearly illustrated in Fig. 1a, while the dc component at 1 kHz shown in Fig. 1c doesn't change significantly compared to that at 100 Hz shown in Fig. 1b. Another important feature in Fig. 1c is that the amplitude decay as a function of harmonic order is faster than that in Fig. 1b: for instance, the amplitude of the second harmonic for 1 kHz is two orders of magnitude smaller than that of the dc component, while for 100 Hz it is only one order of magnitude smaller, indicating that the nonlinearity at high frequencies is weaker than that at low frequencies. This is easily understood: the generation and strength of CDWs corresponding to higher harmonics entirely rely on the nonlinearity originating in the injection-level dependent lifetimes described by Eq. (4). At high frequencies, the CDW amplitude is small, which means that the carrier density and the corresponding carrier lifetimes are modulated within a narrow range, while at low frequencies, the carrier density is modulated within a sufficiently wide range, thereby resulting in much stronger nonlinearity-related effects which manifest themselves as stronger higher harmonics.

With $n(t)$ determined, the time-domain PL signal can be expressed as [43].

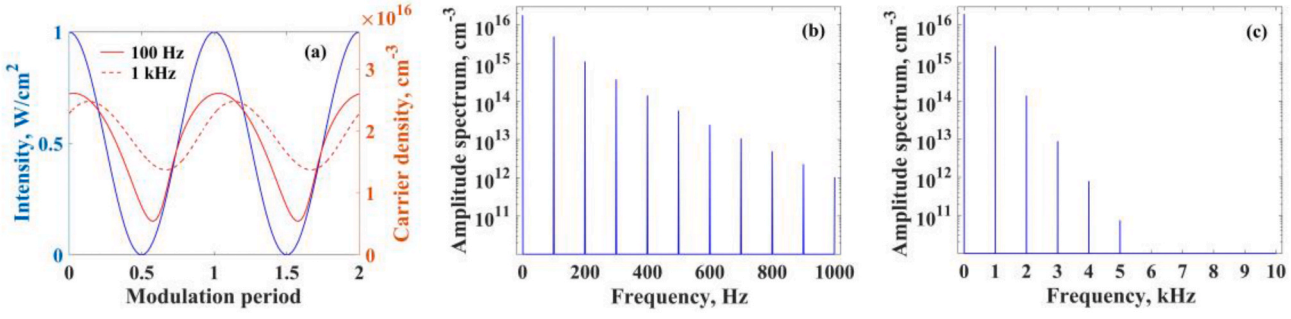

Fig. 1. Solutions of Eq. (16) under 0.5-W/cm^2 808-nm fully-modulated homodyne excitation at 100 Hz and 1 kHz. **(a)** The time-domain excitation waveform (in blue) and the generated carrier density wave $n(t)$ at the two modulation frequencies (in red); **(b)** the amplitude spectrum of $n(t;\omega)$ at 100 Hz excitation; **(c)** the amplitude spectrum of $n(t)$ at 1 kHz excitation. The parameter values used in the simulation are: $L = 290$ μm, $p_0 = 3 \times 10^{15}$ cm^{-3}, $\tau_\mathrm{p} = 1$ ms, $\tau_\mathrm{n} = 5$ ms, $B = 4.73 \times 10^{-15}$ cm^3/s, $C_\mathrm{p} = 10^{-31}$ cm^6/s, $C_\mathrm{n} = 3.8 \times 10^{-30}$ cm^6/s, and $k_\mathrm{max} = 10$.

$$S(t) \propto Bn(t)[n(t)+p_0] \tag{17}$$

Here one can remove the radiative recombination coefficient B from Eq. (17), as it can be absorbed into the proportionality sign which takes into account the surface optical reflectivity of the wafer contributions to the signal, also including the measurement of instrumental factors such as the photon flux detection solid angle. Nevertheless, explicitly retaining B in Eq. (17) is useful for reminding that the PL signal is the result of radiative recombination as represented by the PCR modality. PCR/MPL uses lock-in detection to extract $S(\omega)$, the fundamental frequency component of $S(t)$, as distinct from other frequency components and noise sources [6]. Based on the method of analysis described in Eq. (15), $S(\omega)$ can be expressed in the form of convolution of harmonic CDW components

$$S(\omega) \propto B\left(p_0 n_1 + \sum_{m=-\infty}^{+\infty} n_m n_{1-m}\right) \tag{18}$$

where n_1 means the fundamental frequency CDW. Equation (18) is the final expression for the homodyne PCR/MPL signal, with which the amplitude and phase channels can be calculated, and simulations/best data fits can be carried out by solving Eq. (18) under different excitation intensities and/or different modulation frequencies (see Figs. 2 and 6 as examples). Recall that the two goals of this work are 1) the study of the fully nonlinear PCR/MPL response, and 2) the frequency-domain (spectral) deconvolution of multiplexed optoelectronic CDW de-excitation processes. Therefore, a simulation of the PCR/MPL phase dependence on the injection level (controlled by excitation intensity), shown in Fig. 2, is insightful because a) the variation of lock-in phase with respect to excitation intensity is direct evidence of nonlinearity; and b) the phase dependence from low to high injection levels is dominated by different recombination mechanisms described in Eqs. (5) and (7), a fact which makes it feasible to resolve multiple lifetimes by virtue of spectral measurements of fundamental and higher harmonic CDWs.

The most prominent feature in Fig. 2a is the J-shaped phase (the central part of the solid magenta curve), which is a landmark of the joint effect by SRH, radiative, and Auger recombination processes. Although the J-shaped feature has been widely studied theoretically and experimentally in the semiconductor characterization community [3,5,44], no rigorous theoretical treatment of its origin in "modulated nonlinearity" appears to have been reported, to the best of our knowledge.

To gain an insight into the origins of this J-shaped phase curve, three more curves corresponding to the three separated recombination mechanisms (SRH, blue; radiative, red; and Auger, black) are also shown in Fig. 2. Fig. 2b shows the corresponding effective lifetimes which can be easily calculated from the data in Fig. 2a, using $\tan\phi = -\omega\tau$, where ϕ is the phase [7]. Written as $\tau = -\tan(\phi)/\omega$, this formula is the most intuitive and common way to define the effective carrier lifetime in lock-in techniques. Although this work is attempting to acquire more semiconductor property information than a single effective lifetime which lumps all relaxation effects together, the benefits of the concept of effective lifetime are still there: 1) it is simple to understand and thus popular, 2) it can be relatively simply measured, helping to make an overall quantitative assessment of the sample under investigation; 3) it, or its reciprocal (in the rate dimension), can be used to interpret complicated phenomena in a qualitative but heuristic way. Therefore, the overall effective lifetime and the three separated effective lifetimes are used here to interpret the J-shape feature in Fig. 2 as a result of the competing processes of the three recombination mechanisms. It can be seen from Fig. 2 that the SRH lifetime ranges from 1 ms (τ_p) at low intensities to 6 ms ($\tau_p + \tau_n$) at high intensities, exactly as predicted by Eqs. (5) and (7). The radiative and Auger lifetimes tend to constant values at low intensities and are negatively correlated to intensity at high intensities, with the slope of the former being gentler than that of the latter. This is also predicted by Eqs. (5) and (7). It is well known that in semiconductors the overall effective lifetime is dominated by the shortest among multiple lifetimes [3], and this is why the magenta curve in Fig. 2b appears in that manner: At low intensities, the effective lifetime is dominated by the low limit of the SRH lifetime ($\tau_p = 1$ ms), thereby showing the coincidence between the magenta solid curve and the blue dashed curve. At high intensities the Auger lifetime prevails, accounting for the coincidence between the magenta solid curve and the black dot-dashed curve. By reversing the magenta curve in Fig. 2b, the J-shaped phase curve in Fig. 2a is obtained.

Another feature worth noting in Fig. 2 is that, whether dealing with low or high injection levels in Si, radiative recombination always plays a relatively weak role compared to Auger recombination the lifetime of which is one-order-of-magnitude shorter than the radiative lifetime, owing to the fact that Si is an indirect-bandgap material [36]. This illustrates the point that although PL-based techniques measure radiative signals, those signals carry little information about the radiative recombination lifetime/rate.

2.4. Frequency-domain theory of heterodyne PCR/MPL

PCR/MPL in the heterodyne mode uses two harmonically modulated lasers with a frequency difference to excite free photocarriers in optoelectronic materials with the generation rate

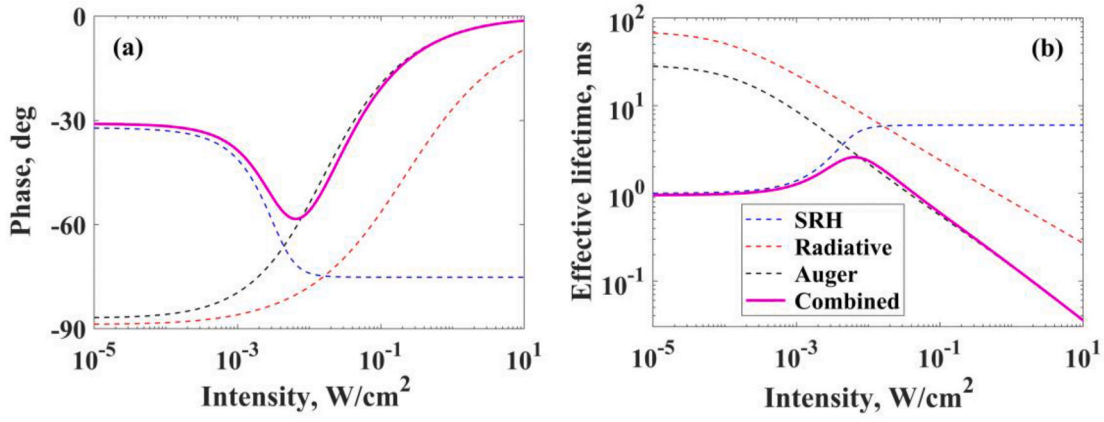

Fig. 2. Simulation of the dependences of **(a)** homodyne PCR/MPL phase at 100 Hz and **(b)** the related effective lifetime on excitation intensity (injection level). The three dashed curves with isolated recombination mechanism were obtained by omitting the other two mechanisms in Eq. (8) during the numerical calculation, while the solid magenta lines are the combined effects. The parameter values used in the simulation are the same as those given in the caption of Fig. 1.

$$G(t)=G_0(1+\cos\omega_1 t+1+\cos\omega_2 t)=G_0\left[2+\frac{1}{2}\left(e^{i\omega_1 t}+e^{-i\omega_1 t}+e^{i\omega_2 t}+e^{-i\omega_2 t}\right)\right] \tag{19}$$

Substituting the above expression for the generation rate in Eq. (11) and solving the resulting coupled system of algebraic equations for each frequency component in a manner similar to the homodyne approach, infinitely many coupled CDW frequency components are generated although there are only two frequency components in the excitation signal. The difference here is that not only the integer multiples of the two frequencies, but also the sum/difference between the two frequencies and their higher harmonics are generated, due to the nonlinear nature of Eq. (11). As a result, one can assume the solution of Eq. (11) in the heterodyne mode to be in the form of a double Fourier series with two summation indices

$$n(t)=\sum_{k_1=-\infty}^{+\infty}\sum_{k_2=-\infty}^{+\infty} n_{k_1,k_2}e^{i(k_1\omega_1+k_2\omega_2)t} \tag{20}$$

Here, $n_{0,0}$ denotes the dc component of $n(t)$ in the heterodyne mode, $n_{0,1}$ denotes the complex amplitude of the ω_2 component, and $n_{-1,1}$ means the complex amplitude of the $\Delta\omega=\omega_2-\omega_1$ component (the beat frequency). Inserting equation (20) into Eq. (11) and writing explicitly the time-derivative term yields

$$\begin{aligned}&A_1\sum_{k_1=-\infty}^{+\infty}\sum_{k_2=-\infty}^{+\infty} n_{k_1,k_2}e^{i(k_1\omega_1+k_2\omega_2)t}+A_2\left(\sum_{k_1=-\infty}^{+\infty}\sum_{k_2=-\infty}^{+\infty} n_{k_1,k_2}e^{i(k_1\omega_1+k_2\omega_2)t}\right)^2\\&+A_3\left(\sum_{k_1=-\infty}^{+\infty}\sum_{k_2=-\infty}^{+\infty} n_{k_1,k_2}e^{i(k_1\omega_1+k_2\omega_2)t}\right)^3+A_4\left(\sum_{k_1=-\infty}^{+\infty}\sum_{k_2=-\infty}^{+\infty} n_{k_1,k_2}e^{i(k_1\omega_1+k_2\omega_2)t}\right)^4=\left(\sum_{k_1=-1}^{+1}\sum_{k_2=-1}^{+1} G_{k_1,k_2}e^{i(k_1\omega_1+k_2\omega_2)t}-\sum_{k_1=-\infty}^{+\infty}\sum_{k_2=-\infty}^{+\infty} i(k_1\omega_1+k_2\omega_2)n_{k_1,k_2}e^{i(k_1\omega_1+k_2\omega_2)t}\right)\\&\times\left(\left(\tau_p+\tau_n\right)\sum_{k_1=-\infty}^{+\infty}\sum_{k_2=-\infty}^{+\infty} n_{k_1,k_2}e^{i(k_1\omega_1+k_2\omega_2)t}+\tau_n p_0\right)\end{aligned} \tag{21}$$

where there are actually five terms in the heterodyne representation Eq. (19) of $G(t)$.

Each frequency component in Eq. (21) must be balanced on both sides of the equal sign, and therefore in a manner similar to Eq. (16), the $\exp[i(k_1\omega_1+k_2\omega_2)t]$ component for all k_1 and k_2 will generate an infinite system of coupled algebraic equations. Again, assuming the truncated order k_{max} corresponding to an acceptable numerical tolerance, the infinite system of equations is reduced to $k_{max}^2+2k_{max}$ complex-valued equations (with the complex conjugate equations excluded). Further reduction of the number of equations to be solved can be achieved by considering the fact that the two excitation angular frequencies ω_1 and ω_2 in the heterodyne mode are adjacent and usually much higher than their difference [26,31], e.g., 1 kHz and 1.01 kHz with a 10 Hz difference which is accessible to NIR cameras for HeLIC imaging. Therefore, it is reasonable to assume that the CDWs at 1 kHz and 1.01 kHz are essentially identical, i.e., $n_{1,0}\approx n_{0,1}$ and thus the equations for ω_2 and its higher harmonics can be merged with those for ω_1 and its respective harmonics.

The time-evolution and the CDW frequency spectra in the heterodyne mode were simulated and are shown in Fig. 3. Compared with the homodyne case, Fig. 3 exhibits much more complicated features.

In Fig. 3a, the blue curve denotes the excitation beat waveform which is proportional to the generation rate $G(t) = G_0(2+\cos\omega_1 t + \cos\omega_2 t)$. The envelope (beat) period in Fig. 3a is 0.2 s, containing 20 periods of the 100-Hz component and 22 periods of the 110-Hz component. The envelope is a reflection of the 10-Hz difference between the two frequencies. The carrier density wave solution $n(t)$ shown in Fig. 3a (red) seems, at first sight, similar to the excitation curve, however, from Fig. 3b one can see that its frequency content is much more complicated, due to the nonlinear nature of Eq. (8). Three important frequency components are highlighted as different color symbols, as described in the caption of Fig. 3. The most important component in heterodyne excitation is the $\Delta\omega$ beat component $n_{-1,1}$. In Fig. 3b, the amplitude of $n_{-1,1}$ is less than that of the dc and the two fundamental components, but is on the same order of magnitude as that of the 2 s harmonics $2\omega_1$ and $2\omega_2$. This can be understood as follows: The generation of the dc and the two fundamental components in $n(t)$ can be treated as first-order effects, because there are dc and two fundamental

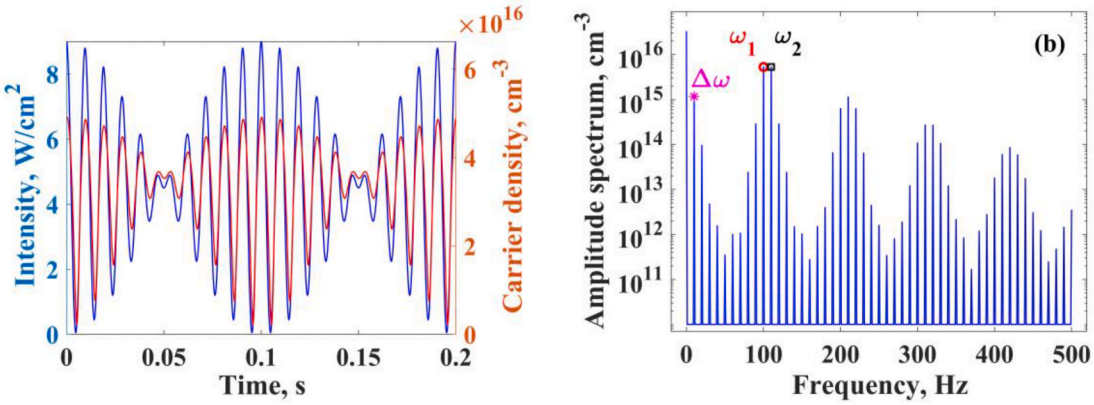

Fig. 3. Solutions of Eq. (21) under 4.5-W/cm^2 808-nm 100-Hz & 110-Hz heterodyne excitation. **(a)** The time-evolution excitation waveform (blue) and the generated carrier density wave $n(t)$ (red); **(b)** the amplitude spectrum of $n(t)$, with the red circle and the black square denoting the fundamental of ω_1 and ω_2, respectively. The magenta asterisk denotes the 10-Hz beat frequency. The parameters used in the simulation are: $L = 680$ μm, $p_0 = 3\times10^{14}$ cm^{-3}, $\tau_p+\tau_n = 380$ μs, $B = 4.73\times10^{-15}$ cm^3/s, $C_p+C_n = 1.85\times10^{-30}$ cm^6/s, and $k_{max} = 10$.

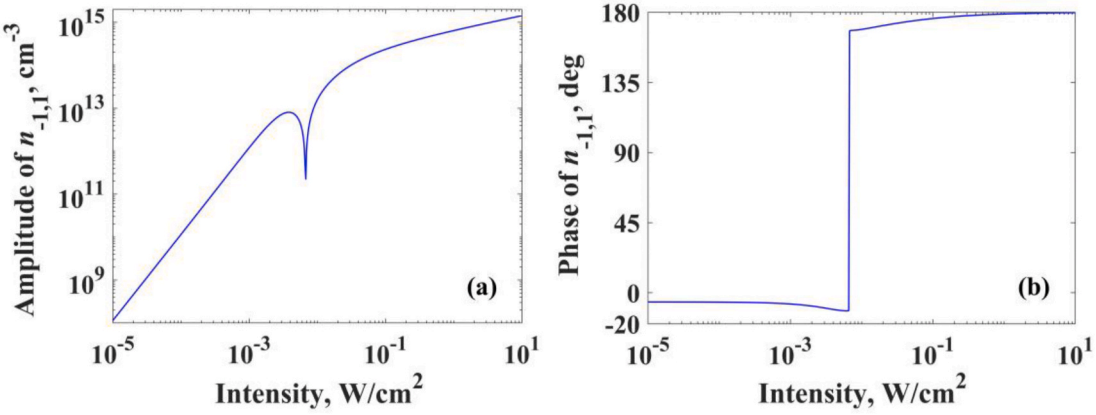

Fig. 4. (a) The amplitude and **(b)** the phase of the $n_{-1,1}$ term vs. intensity, based on the solution of Eq. (21). The material parameters were the same as those used in Fig. 1.

components in the driving source term $G(t)$. Next, the existence of the beat frequency and the 2 s harmonics can be regarded as second-order effects, results of frequency mixing operations: the self-multiplication of the ω_1 term yields the second harmonic, and the ω_1, ω_2 mixing multiplication generates the beat term. All other frequency components in Fig. 3b can be classified as higher-order effects, the results of further self- and cross-multiplications of the fundamental modes. It is seen that the higher the order the lower the amplitude, a fact that shapes the appearance of the spectrum in Fig. 3b. Since the beat frequency and the 2 s harmonics are second-order effects, they are expected to have similar amplitudes, but less than those of the dc and the two fundamental components.

Heterodyne PCR/MPL uses lock-in detection with the reference frequency set at $\Delta\omega$ to extract $S(\Delta\omega)$. Inserting Eq. (20) into Eq. (17) yields

$$S(t) \propto n(t)[n(t)+p_0] = \sum_{k_1=-\infty}^{+\infty}\sum_{k_2=-\infty}^{+\infty} n_{k_1,k_2} e^{i(k_1\omega_1+k_2\omega_2)t}\left(\sum_{k_1=-\infty}^{+\infty}\sum_{k_2=-\infty}^{+\infty} n_{k_1,k_2} e^{i(k_1\omega_1+k_2\omega_2)t}+p_0\right) \quad (22)$$

The heterodyne PCR/MPL signal at $\Delta\omega$ extracted from the full heterodyne frequency spectrum is

$$S(\Delta\omega) \propto 2n_{-1,0}n_{0,1} + (2n_{0,0}+p_0)n_{-1,1} \quad (23)$$

There are two terms on the rhs of Eq. (23): The first term is at the beat frequency ω_2–ω_1; the second term is also at the beat frequency because the beat component $n_{-1,1}$ multiplies dc terms (both $n_{0,0}$ and p_0) thereby remaining at the beat frequency. The two terms are both complex quantities and generate amplitude and phase signals upon lock-in demodulation. The sum of the two complex terms can be regarded mathematically as a vector summation, or physically as interference between two CDWs. The relative phase between the two interfering CDWs is very important to the resultant signal: When the phase difference between the two CDWs is zero, their superposition can be regarded as constructive interference; and when the phase difference is 180 deg, the interference is destructive. If the amplitudes of the two CDWs happen to be close and the phase difference is 180 deg, a fully destructive interference will occur.

The phase of the first term on the rhs of Eq. (23) is always close to zero because in the heterodyne mode the two frequencies are adjacent, thereby rendering the CDWs at ω_1 and ω_2 essentially the same, i.e., $n_{1,0} \approx n_{0,1}$. Therefore, $n_{-1,0}$, the complex conjugate of $n_{1,0}$, multiplied by $n_{0,1}$ must yield a phase difference close to zero degree. However, the phase of the second term $n_{-1,1}$ depends on many factors such as the excitation intensity and the optoelectronic transport properties of the specific electronic material. Fig. 4 shows how the amplitude and the phase of the $n_{-1,1}$ term change with the laser excitation intensity.

At low injection levels where the SRH lifetime dominates (the monotonically increasing part of the solid magenta curve shown in Fig. 2b), the phase of $n_{-1,1}$ is close to zero; at high injection levels where the Auger lifetime prevails (the monotonically decreasing part of the solid magenta curve shown in Fig. 2b), the phase of $n_{-1,1}$ is close to 180 deg (the same is true for radiative recombination but its influence on the final signals is much weaker than that of Auger recombination in Si). In Fig. 4b there is a phase transition at a specific intensity which manifests itself as a local sharp minimum value (a "notch") in the amplitude vs. intensity dependence shown in Fig. 4a. This critical point is the recombination outcome of competition between SRH and Auger nonlinearities: below that point, the generation of $n_{-1,1}$ is mainly due to the SRH nonlinearity and the two CDWs described by Eq. (23) coexist in constructive interference; above the point, the generation of $n_{-1,1}$ is dominated by the Auger mechanism and therefore the interference becomes destructive, as $n_{-1,1}$ generated by the Auger nonlinearity has a 180-deg phase.

3. Experimental

A schematic of the homodyne PCR/MPL experimental system is shown in Fig. 5. An 808-nm fiber-coupled semiconductor laser with 18-W peak power was internally modulated by a function generator and used as the optical excitation source, with the modulation amplitude factor $\gamma = 1$ for the full-modulation mode and $\gamma = 0.1$ for the ripple excitation mode, controlled by the electrical signal from the function generator. The laser beam was first collimated, then spread and homogenized by a diffuser to cover a 4×4 cm^2 area on wafer samples. In the laser beam path between the collimator and the diffuser, an iris and brass grids were added so that the excitation intensity could be continuously changed over a wide range through adjusting the iris and adding brass grids (50% transmittance for each), but the intensity distribution (uniformity) on the sample surface was not changed by virtue of the diffuser. The sample temperature rise under these illumination levels was roughly estimated to be less than 30 °C, so the influence of temperature on the sample electronic properties was neglected. Diffuse PL signals from the sample were collected and collimated with two off-axis paraboloidal mirrors and focused onto an InGaAs detector (spectral detection range 900–1700 nm) with long-pass filters placed in front of it in order to block the excitation beam. Another InGaAs detector was used to monitor the relative change of the 808-nm excitation intensity by measuring the reflected beam from the sample front surface, while the absolute intensity was measured using a power meter placed at the position of the sample. Two lock-in amplifiers demodulated the detector output signals and provided amplitude and phase information. The time constant of both lock-in amplifiers was set at 1 s.

The heterodyne PCR/MPL system was based on the abovementioned homodyne system but with some modifications: One more laser of the same type was added and modulated at ω_2 by the same two-channel

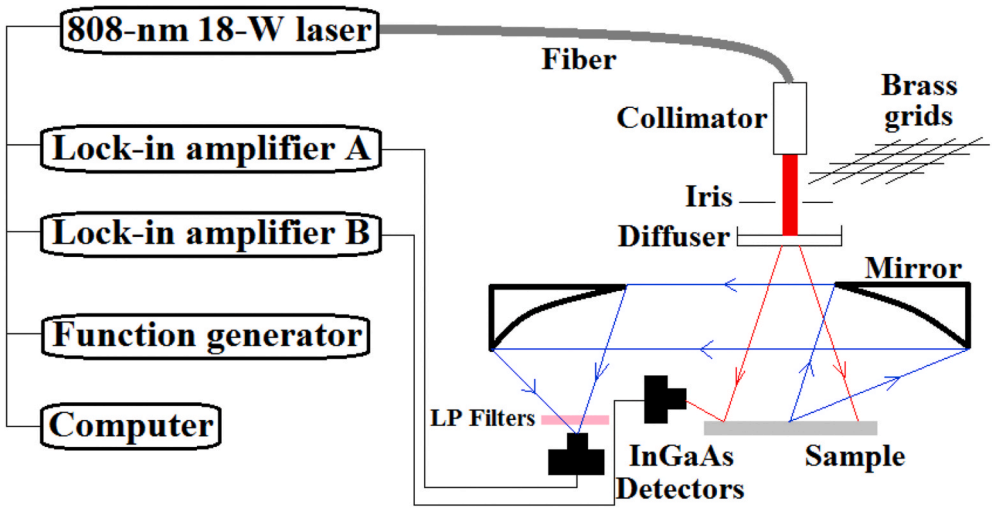

Fig. 5. Experimental setup for homodyne PCR/MPL measurements.

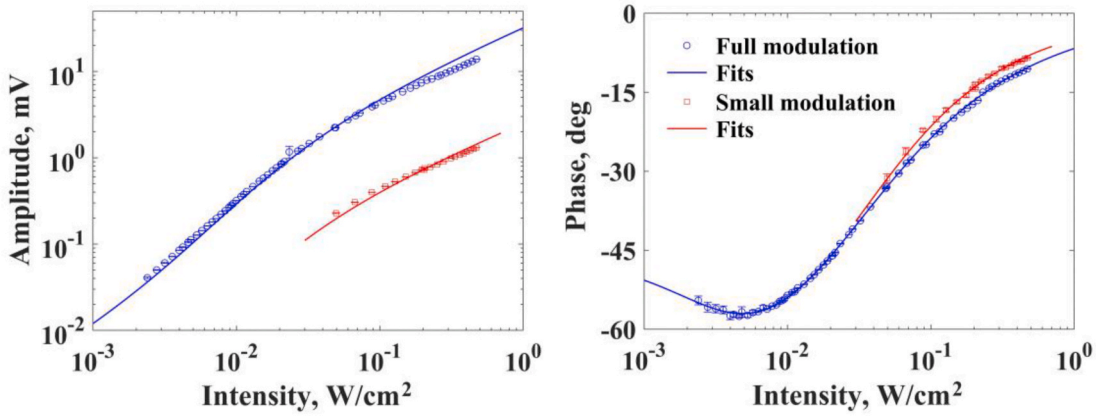

Fig. 6. Homodyne 100-Hz PCR/MPL intensity-scan data of Sample No. 1 and the corresponding theoretical best fits using Eq. (18) and the solution of Eq. (16). **(a)** Amplitude, and **(b)** phase. The blue data are in the full-modulation mode, while the red data are in the ripple mode with $\gamma = 0.1$. The best-fitted parameters are the doping density $N_D = (2.60 \pm 0.04) \times 10^{15}$ cm^{-3}, $\tau_p = 1.90 \pm 0.05$ ms, $\tau_n = 4.0 \pm 0.1$ ms, $B = (2.7 \pm 0.4) \times 10^{-14}$ cm^3/s, $C_p = (1.0 \pm 0.4) \times 10^{-31}$ cm^6/s, and $C_n = (1.40 \pm 0.03) \times 10^{-30}$ cm^6/s.

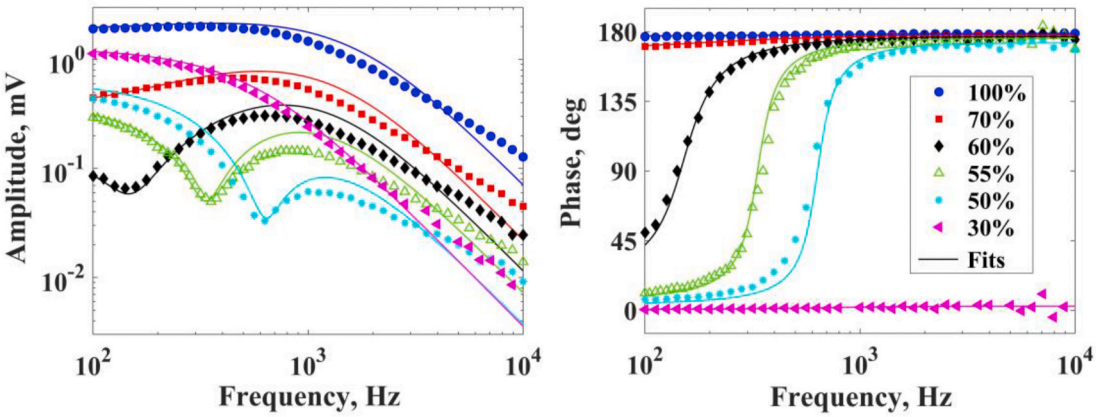

Fig. 7. Heterodyne modulation-frequency-scan data with $\Delta f = 10$ Hz of Sample No. 2 at six different intensities and the corresponding theoretical best fits using Eq. (23) and the solution of Eq. (21). **(a)** Heterodyne amplitude, and **(b)** heterodyne phase. The 100% intensity corresponds to 4.5 W/cm^2. Symbols denote experimental data, and solid curves represent theoretical fits. Experimental data and theoretical curve at the same intensity have the same color. The best-fitted parameters are $\tau_p + \tau_n = 380 \pm 0.5$ μs, $B = (5.05 \pm 0.05) \times 10^{-15}$ cm^3/s, and $C_a = C_p + C_n = (1.85 \pm 0.01) \times 10^{-30}$ cm^6/s. The equilibrium majority carrier density during fitting was fixed at $p_0 = 3 \times 10^{14}$ cm^{-3}. The reason that only the sums of the two SRH time constants and the two Auger coefficients can be obtained is that high-injection condition, Eq. (7), held throughout these measurements.

function generator. An extra data acquisition card was used to generate the $\Delta\omega$ beat frequency reference signal for the lock-in amplifier and extract the $\Delta\omega$ component from PCR/MPL signals. Synchronization of the system was controlled by a LABVIEW program.

Two Cz c-Si wafers were tested: sample No. 1 was n-type, 290-μm thick, with both surfaces passivated with a 30-nm amorphous-Si (α-Si) layer, and 1 Ω cm nominal resistivity provided by the manufacturer; sample No. 2 was p-type, 680-μm thick, with both surfaces passivated with thick oxides, and 20–40 Ω cm nominal resistivity also provided by the manufacturer. Sample No. 1 features long effective lifetime by virtue of the highly efficient α-Si surface passivation as well as a relatively low resistivity. Therefore, a broad carrier-injection range covering the two limits described by Eqs. (5) and (7) can be fulfilled for sample No. 1, based on the abovementioned experimental system. This renders the homodyne phase dependence of sample No. 1 on the excitation intensity exhibiting the *J*-shaped feature as already simulated and discussed in Fig. 2, from which the six key electronic parameters can be extracted uniquely, as shown in Fig. 6. Sample No. 2 was chosen because its heterodyne frequency-scan responses under the available excitation intensities of the experimental system constitute a complete set of data to clearly illustrate the full spectrum of behavior of the notch phenomenon, as shown in Fig. 7.

4. Results and discussion

A homodyne PCR/MPL intensity-scan experiment was performed to corroborate the simulation shown in Fig. 2. The experimental amplitude and phase dependencies on the excitation intensity and the corresponding theoretical best fits using Eq. (18) and the solution of Eq. (16) are shown in Fig. 6. The truncated order was set at $k_{max} = 10$ for all data analyses.

The variation of lock-in phase with respect to excitation intensity shown in Fig. 6b is direct evidence of nonlinearity. A smaller phase lag means a shorter effective lifetime and a faster recombination rate. The *J*-shaped phase is consistent with the theoretical prediction shown in Fig. 2a, which is a manifestation of the joint effects of SRH (dominating the low intensity region), radiative, and Auger recombination (dominating the high intensity region) processes. The deviation of the phase data between the full modulation (blue circles) and the ripple modulation (red squares) is another evidence of nonlinearity, as phase should be independent of modulation amplitude in linear systems. The *x*-axis label "intensity" in Fig. 6 should be perceived as the averaged intensity, independent of full or ripple modulation. From Fig. 6a, the ripple-mode amplitudes are basically 10 times less than those of the full-modulation mode at the same intensities, as expected from setting $\gamma = 0.1$, while in Fig. 6b the ripple phases are consistently smaller than those of the full-modulation mode, an indication of shorter effective lifetime in the ripple mode. This is due to the fact that the excitation intensity range corresponding to the ripple-mode data has already entered into the Auger-recombination dominated regime. Consequently, compared to the full modulation mode where the carrier density is modulated from low to high, the ripple-mode carrier density is maintained at a relatively high level. In the measurement, the ripple-mode intensity-scan range is not as wide as that in the full-modulation mode, as the 10-fold reduced signal amplitude leads to lower SNR.

The six to-be-fitted parameters are the doping density N_D (also the equilibrium free electron density since sample No. 1 is n-type; here N_D is used instead of n_0, the latter already being used to denote the dc component of the excess carrier density), the two SRH time constants τ_p and τ_n, the radiative recombination coefficient B, and the two Auger recombination coefficients C_p and C_n. The best-fitted values are shown in the caption of Fig. 6. The best fitting procedure was executed once for the whole set of data shown in Fig. 6, both amplitude and phase, and with both full- and ripple-modulation data; in other words, the developed best-fitting program was able to simultaneously analyze the whole set of data under different experimental conditions, which can highly suppress the non-uniqueness problem often encountered in multiparameter fitting and thus guarantee reliability of the best-fit output.

The best-fitted equilibrium majority carrier density value $N_D = 2.6 \times 10^{15}$ cm^{-3} corresponds to a resistivity value of 1.8 Ω cm using the empirical formulas given in Ref. [3] which is consistent with the nominal resistivity provided by the wafer manufacturer. The best-fitted τ_p and τ_n values are milliseconds long, a result of high effectiveness of α-Si surface passivation which highly suppresses surface recombination (a form of SRH recombination). The best-fitted value $B = 2.7 \times 10^{-14}$ cm^3/s is about 1.5 times higher than the value reported by Gerlach et al. [45] and 4 times higher than that reported by Trupke et al. [46]. It must be noted that during this multi-parameter fitting, the sensitivity of B is the lowest among the six parameters, because radiative recombination always plays a relatively weak role in Si compared to Auger recombination, the lifetime of which is one-order-of-magnitude shorter than the radiative lifetime, as already discussed in the simulation shown in Fig. 2.

The most cited values of the two Auger recombination coefficients of Si [47] are $C_n = 2.8 \times 10^{-31}$ cm^6/s and $C_p = 0.99 \times 10^{-31}$ cm^6/s. While the best-fitted C_p value in this work, shown in the caption of Fig. 6, is in excellent agreement with the most cited value, the best-fitted C_n value is approx. 4 times higher. However, the authors of Ref. [47] emphasized that their measured values hold only for the case where either the doping density or the injected carrier density is no less than 10^{18} cm^{-3}, so investigators who cited these two values may have actually mistaken the applicability of these results. For medium or lightly doped c-Si and for carrier injection levels lower than 10^{18} cm^{-3} (the present case), a recent study [44] shows that, due to the effect of Coulomb-enhanced Auger recombination [48], the two Auger coefficients given in Ref. [47] must be multiplied by two parameters called the Coulomb-enhanced factors [44], respectively. According to Eq. (19) of Ref. [44] and using the equilibrium majority carrier density value determined in this work, the enhancement factor g_{eeh} was estimated to be 13.5, and the modified C_n value should be $C_n = 3.8 \times 10^{-30}$ cm^6/s. Therefore, the $C_n = 1.4 \times 10^{-30}$ cm^6/s value determined in this work is 1.7 times lower than the corrected Coulomb-enhanced value.

Next, a heterodyne PCR/MPL frequency-scan experiment at six different intensities was performed and the results are shown in Fig. 7. The *x*-axis label "frequency" denotes the modulation frequency of the first laser, f_1, while the second laser was modulated at $f_2 = f_1 + 10$ Hz, and the amplitudes and the phases shown in Fig. 7 are lock-in demodulated at 10 Hz.

The data shown in Fig. 7 illustrate the behavior of an abnormal notch (amplitude depression) phenomenon observed in our HePCR/MPL measurements. The frequency response at maximum intensity (labeled "100%") shows an "ordinary" amplitude behavior and almost constant phases close to 180 deg. The data at 70% intensity can be regarded as the onset of the notch phenomenon: Although within the frequency window there is no amplitude depression, just a mild non-monotonic response, it can be inferred that the notch at this intensity may reside in a lower frequency range. For 60%, 55%, and 50% intensities, the notch clearly emerges and its frequency location shifts rapidly from 100 Hz to 600 Hz. This notch phenomenon has not only been observed in this sample, but also in HeLIC measurements of mc-Si solar cells and other semiconductor materials and devices such as Si solar cells and CdZnTe compounds used for infrared focal plane array detectors. For 30% intensity, the notch almost disappears and its amplitude frequency response resumes "ordinary" behavior while its phase undergoes a 180-deg shift with respect to the 100% intensity response.

The theoretical best-fitting results are also shown in Fig. 7 as solid curves with different colors. The developed program is capable of simultaneously best fitting the entire set of data shown in Fig. 7, with the six intensities entered as known parameters. The simultaneous fitting software searches for only one set of carrier recombination parameters which can best fit all six experimental data curves. Here, simultaneous fitting is necessary because among the six experimental data curves the only varied parameter was the laser intensity. Although some

semiconductor properties such as the effective carrier lifetime are functions of laser intensity (actually of excess carrier density), those introduced in Eq. (8) *do not depend* on experimental parameters: the radiative coefficient and the Auger coefficients are intrinsic properties of c-Si and thus should be independent of laser intensity, while the two SRH time constants are related to thermal carrier velocities and carrier capture cross sections of the recombination centers, also independent of laser intensity. Fig. 7 shows that the simultaneous best-fitting of the entire set of data at the six different intensities is good, especially in terms of phase. The observed heterodyne phase behavior being close to 180 deg at 100% intensity and switching to near 0 deg at 30% intensity is consistent with the theory. The 70% intensity phase data constitute the onset of the notch phenomenon, with a small phase deviation from 180 deg at low frequencies. For 60%, 55%, and 50% intensities, the phases undergo transitions from 0 to 180 deg, indicating that at low frequencies the first term in Eq. (23) prevails whereas high frequencies are dominated by the second term.

The best-fitted parameters are given in the caption of Fig. 7. The reason for which only the sums of the two SRH time constants and the two Auger coefficients can be obtained is that sample No. 2 is a high-resistivity wafer compared to sample No. 1, and its equilibrium majority carrier density is around $p_0 = 3 \times 10^{14}$ cm^{-3}, much lower than the injected photocarrier density. Therefore, the high-injection condition described by Eq. (7) held throughout this measurement. The sum of the two SRH time constants $\tau_p + \tau_n = 380$ μs is approximately one-order-of magnitude shorter than that of sample No. 1, due to the less efficient surface passivation of the thick oxide than the α-Si [30]. The radiative recombination coefficient value $B = 5.05 \times 10^{-15}$ cm^3/s is less than that of sample No. 1, but is very close to the value $B = 4.73 \times 10^{-15}$ cm^3/s reported by Trupke et al. [46]. The measured ambipolar Auger coefficient value $C_a = 1.85 \times 10^{-30}$ cm^6/s for sample No. 2 is very close to that of sample No. 1. In principle, unlike the SRH lifetime which generally differs among different c-Si samples, the radiative and Auger recombination coefficients do not vary significantly for lightly doped c-Si, due to the fact that these two recombination processes are intrinsic in contrast to the extrinsic nature of SRH recombination.

Fig. 7a shows that the notch center positions of the theoretical curves are in excellent agreement with the experimental results, however, the amplitude best fits at high frequencies are inadequate as the theoretical predictions decrease faster than the experiments. This might be due to some inherent features of the theory: Equation (8) is a rate equation which doesn't take carrier diffusion into account. As already discussed in Section 2, the carrier density $n(t)$ in Eq. (8) should be perceived as a spatially-averaged (especially depth averaged) carrier density. In view of the strongly nonlinear nature of the problem, this spatial averaging may cause the rate theory to diverge from experimental behavior, especially for thick samples and/or high frequencies where the ac carrier diffusion length becomes shorter and the spatial inhomogeneity of the carrier density distribution due to diffusion along the depth becomes considerable. To rigorously address this problem, one needs to solve the initial- and boundary-value problem of Eq. (1) instead of Eq. (8). However, given the much more complicated mathematical structure of Eq. (1a) and in view of the excellent prediction of the notch positions in Fig. 7, this theoretical improvement will be left for a future study.

The uncertainties of the determined parameter values of the two samples are also shown in the captions of Figs. 6 and 7. The way to estimate the uncertainties is as follows. First, the following two quantities need to be calculated and compared

$$\begin{cases} X_1 = \sqrt{\sum_{j=1}^{N} \left(y_j^{\text{th}} - y_j\right)^2} \\ X_2 = \sqrt{\sum_{j=1}^{N} \sigma_j^2} \end{cases} \tag{24}$$

where N is the number of experimental data used in a best-fitting, yth is the theoretical best-fitted value (amplitude or phase), y^{exp} is the measured experimental data value, and σ is the corresponding standard deviation of the measurement. Each datum was measured 9 times in our experiments, with $y^{\text{exp}}{}_j$ being the mean value and σ_j the corresponding standard deviation, manifesting itself as an errorbar associated with each data symbol in Fig. 6. It is clear that X_1 is the deviation between theory and experiment (the fitting used a least-square algorithm) and thus is a quantization of the quality of the best-fitting, while X_2 is a quantization of the quality (uncertainty) of the experimental data.

The case $X_1 < X_2$ means that the deviation between theory and experiment is already within the uncertainty of the experimental data, and so, there is no need to further seek "better" parameter values to improve the fitting quality. Sample No. 1 belongs to this case: the X_1 value corresponding to the best-fitted theoretical curves shown in Fig. 6 is about 1.5 times smaller than X_2. Therefore, to estimate the uncertainties of the determined six parameter values of sample No. 1, we intentionally made the six parameters deviating from their best-fitted values, respectively, which surely resulted in larger X_1. Using X_2 as a criterion, when $X_1 \approx X_2$, we treated the deviation of a specific parameter as the uncertainty of the parameter in this measurement.

On the other hand, the case $X_1 > X_2$ means the fitting is insufficient. This may be caused by either the best parameter values have not yet found, or there is inherent discrepancy between the theoretical model and the measured data. Sample No. 2 belongs to this case: the X_1 value corresponding to the best-fitted theoretical curves shown in Fig. 7 is about 4 times larger than X_2. By further seeking other parameter values, there was no considerable improvement found. As discussed above, this can be attributed to the insufficiency of the current model due to the spatial averaging treatment. Therefore, to estimate the uncertainties of the determined parameter values of sample No. 2, we used the minimum numerical steps of parameter values in the best-fitting procedure as the uncertainties of this measurement.

Based on the results shown in Fig. 7, the injected carrier densities at the six intensities were further calculated. It was found that under heterodyne excitation, the injected carrier density is modulated in a rather complicated manner. Fig. 8 presents the dc levels of the $n(t)$ distributions at the same frequencies and intensities shown in Fig. 7 that produce rough estimates of the dc levels of the injected CDWs. In Fig. 8 it is observed, even for a single intensity, that the dc levels of the CDWs $n(t)$ are not constant, but exhibit variations on the order of 10^{16} cm^{-3}. The fact that the dc carrier density levels are a function of modulation

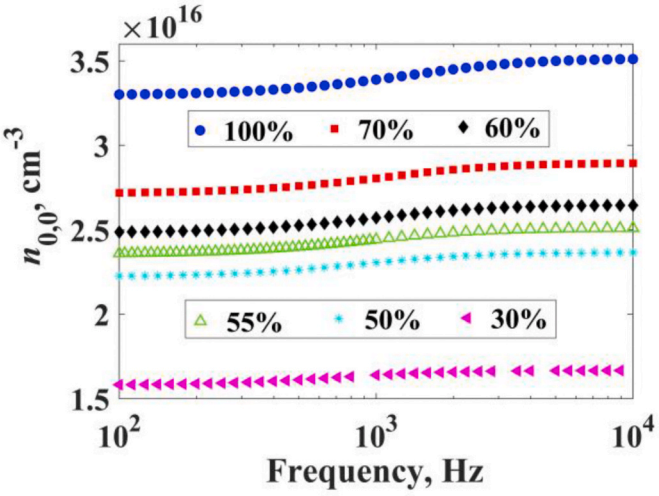

Fig. 8. The calculated dc levels of the CDWs at the same frequencies and intensities as shown in Fig. 7. The calculation was based on the extracted parameters shown in the caption of Fig. 7.

Table 1
Extracted multiple lifetimes based on the results shown in Figs. 7 and 8.

Lifetime	Mechanism	100%	70%	60%	55%	50%	30%
No. 1	SRH	380 μs					
No. 2	Radiative	5.74 ms	6.93 ms	7.56 ms	8.01 ms	8.42 ms	11.8 ms
No. 3	Auger	454 μs	662 μs	788 μs	885 μs	978 μs	1.92 ms
Effective	Combined	156 μs	184 μs	196 μs	204 μs	212 μs	266 μs

frequency is a natural consequence of the nonlinear frequency mixing and a result of the different CDW modulation depths.

Based on the carrier density information shown in Fig. 8, the three extracted fundamental parameters can be transformed into the form of "multiple lifetimes" in order to gain an insight into the advantage of the heterodyne PCR/MPL methodology's capability to deconvolute multiplexed optoelectronic relaxation processes. The reason that the heterodyne notch helps resolve the multiple parameters more reliably is that the frequency response curves with a notch exhibit more specific features in both amplitude and phase channels than those without. The features originate in destructive interference among the carrier density waves generated by the different recombination mechanisms, as described in Fig. 4 and the associated text, a physical effect which brings high sensitivity to the resolution of the parameters corresponding to the different recombination mechanisms. The outcomes are shown in Table 1.

In view of the fact that the aforementioned three recombination mechanisms were used to interpret the data, three lifetimes were identified, i.e., the SRH, radiative and Auger lifetime. The extracted SRH lifetime value, $\tau_p + \tau_n$, shown in the caption of Fig. 7 is constant among the six-intensity data, as the high-injection conditions, Eq. (7), were dominant throughout the experiments. From Equation (7) it can be seen that at high injection levels, the radiative and the Auger lifetimes are negatively correlated with the injected CDW. Based on the results shown in Fig. 8, the average of each dc level was used to estimate the corresponding radiative and Auger lifetimes, as shown in Table 1. The last row of Table 1 is the effective lifetime which lumps all the recombination mechanisms together. The effective lifetime is the parameter that most other lifetime techniques can provide, however, the analytical method developed in this work can further deconvolute the lifetimes corresponding to various operating physical mechanisms, a fact which paves the way for allowing semiconductor optoelectronic materials scientists and device developers to evaluate limiting factor(s) detrimental to photocarrier transport properties, thereby linking substrate property optimization and device fabrication process details toward optimal device performance.

5. Conclusions and outlook

This study developed an analytical method which can be used for describing nonlinear photocarrier recombination dynamics in semiconductors, with a specific example focus on c-Si, and for investigating the frequency response of nonlinear systems under harmonic excitation in general, both in homodyne and heterodyne PCR/MPL modes. Two carefully selected sets of PCR/MPL experimental data exhibiting newly observed modulation-frequency induced phenomena, a homodyne intensity-scan response with *J*-shaped phase and a heterodyne frequency-scan response with an amplitude depression ("notch") and a 180-degree phase transition, were used to corroborate, and be interpreted by, the developed nonlinear rate theory. Homodyne intensity-scan experimental results corroborated the theoretical predictions, and six key electronic parameters of a c-Si wafer, i.e. the doping density, the two Shockley-Read-Hall time constants, the radiative recombination coefficient, and the two Auger recombination coefficients, were simultaneously extracted through best fitting the theory to the experimental data. Overall, theory and experiment showed very good agreement, highlighted by the accurate prediction of the center frequency location of heterodyne amplitude notches and the derivation of best-fitted parameter values consistent with literature reports. An observed deviation of the heterodyne amplitudes between theory and experiment at high frequencies was analyzed and its potential origins in terms of the absence of diffusion from the CDW processes was discussed.

Furthermore, the abnormal notch phenomenon was successfully described by the developed theory quantitatively and was interpreted as the result of destructive interference between carrier-density waves generated from different sources of nonlinearity. On one hand, this study can provide a deeper understanding of the complicated nonlinear carrier dynamics in semiconductors through PCR/MPL measurements. On the other hand, it establishes the foundations of nonlinear Fourier analysis for camera-based homodyne and heterodyne LIC-based imaging techniques to achieve spatially and temporally resolved quantitative deconvolution of optoelectronic relaxation processes in time-multiplexed systems.

The experimental and theoretical methods proposed in this manuscript can be extended to the characterization of other semiconductors including direct-band materials. Experimentally, excitation lasers emitting at different wavelengths are needed for different direct-band materials in order to generate excess photocarriers. At the same time, photodetector(s) with appropriate spectral responses are needed for luminescence detection, equipped with appropriate optical filter(s) placed in front of the detector to eliminate the excitation beam while letting PL signals pass. Experimentally, a wide range of modulation frequencies must be accessible in view of the fact that the carrier recombination lifetimes in direct-band materials are usually on the order of sub-μs, and this may be a technical challenge for today's lasers in terms of both large modulation bandwidth and high power (required for spreading the beam for imaging purposes). These are the kinds of changes required for addressing other types of semiconductors but they are not limitations of the methodology itself. Theoretically, due to the fact that the time scale under investigation is much shorter for the case of direct-band semiconductors, caution needs to be paid to the simplifications employed in this manuscript, such as the charge neutrality approximation. However, as long as the mathematical rate equations corresponding to specific recombination dynamics are established (for example, in the presence of intra-bandgap nonlinear carrier trapping kinetics), the same frequency-domain theoretical treatment on the nonlinearities and the corresponding computational and analysis method can be used directly.

Author statement

Qiming Sun: Conceptualization, Methodology, Formal analysis, Visualization, Original draft preparation, Alexander Melnikov: Software, Validation, Andreas Mandelis: Supervision, Conceptualization, Methodology, Writing-Reviewing and Editing, Yaqin Song: Investigation, Validation.

Declaration of competing interest

The authors declare that they have no known competing financial interests or personal relationships that could have appeared to influence the work reported in this paper.

Acknowledgments

The authors are grateful to the Natural Sciences and Engineering Research Council of Canada (NSERC) for a Discovery grant, to the Canada Foundation for Innovation (CFI) for equipment grants, to the Canada Research Chairs Program, and to the Chinese Recruitment Program of Global Experts (Thousand Talents). QMS acknowledges the NSFC (Grant Nos. 61771103, 61601092, & 61704023). YQS

acknowledges the NSFC (Grant No. 11672224) and financial support from the program of China Scholarships Council (201806285044).

References

[1] S. Rein, Lifetime Spectroscopy: A Method of Defect Characterization in Silicon for Photovoltaic Applications, Springer-Verlag Berlin Heidelberg, 2005.
[2] S.M. Sze, K.K. Ng, Physics of Semiconductor Devices, third ed., John Wiley & Sons, NJ, 2007.
[3] D.K. Schroder, Semiconductor Material and Device Characterization, third ed., John Wiley & Sons, NJ, 2006.
[4] T. Trupke, R.A. Bardos, M.D. Abbott, Self-consistent calibration of photoluminescence and photoconductance lifetime measurements, Appl. Phys. Lett. 87 (2005) 184102.
[5] J. Giesecke, Quantitative Recombination and Transport Properties in Silicon from Dynamic Luminescence, Springer PhD Theses, 2014.
[6] A. Mandelis, J. Batista, D. Shaughnessy, Infrared photocarrier radiometry of semiconductors: physical principles, quantitative depth profilometry, and scanning imaging of deep subsurface electronic defects, Phys. Rev. B 67 (2003) 205208.
[7] Q.M. Sun, A. Melnikov, A. Mandelis, Quantitative self-calibrating lock-in carrierographic lifetime imaging of silicon wafers, Appl. Phys. Lett. 101 (2012) 242107.
[8] R.N. Hall, Electron-hole recombination in germanium, Phys. Rev. 87 (1952) 387.
[9] W. Shockley, W.T. Read, Statistics of the recombinations of holes and electrons, Phys. Rev. 87 (1952) 835–842.
[10] D. Guidotti, J.S. Batchelder, A. Finkel, J.A. Van Vechten, First-overtone response in modulated photoluminescence emission in silicon at room temperature, Phys. Rev. B 38 (1988) 1569–1572.
[11] D. Guidotti, J.S. Batchelder, A. Finkel, P.D. Gerber, J.A. Van Vechten, Modeling of luminescence phase delay for nondestructive characterization of Si wafers, J. Appl. Phys. 66 (1989) 2542–2553.
[12] A. Mandelis, Y. Riopel, Laser infrared photothermal radiometry of electronic solids: principles and applications to industrial semiconductor Si wafers, J. Vac. Sci. Technol. A 18 (2000) 705–708.
[13] A. Melnikov, A. Mandelis, J. Tolev, P. Chen, S. Huq, Infrared lock-in carrierography (photocarrier radiometric imaging) of Si solar cells, J. Appl. Phys. 107 (2010) 114513.
[14] J. Batista, A. Mandelis, D. Shaughnessy, Temperature dependence of carrier mobility in Si wafers measured by infrared photocarrier radiometry, Appl. Phys. Lett. 82 (2003) 4077–4079.
[15] D. Shaughnessy, B.C. Li, A. Mandelis, J. Batista, Ion implant dose dependence of photocarrier radiometry at multiple excitation wavelengths, Appl. Phys. Lett. 84 (2004) 5219–5221.
[16] B.C. Li, D. Shaughnessy, A. Mandelis, J. Batista, J. Garcia, Three-layer photocarrier radiometry model of ion-implanted silicon wafers, J. Appl. Phys. 95 (2004) 7832–7840.
[17] A. Melnikov, A. Mandelis, B. Halliop, N.P. Kherani, Effective interface state effects in hydrogenated amorphous-crystalline silicon heterostructures using ultraviolet laser photocarrier radiometry, J. Appl. Phys. 114 (2013) 244506.
[18] Y.C. Zhang, A. Melnikov, A. Mandelis, B. Halliop, N.P. Kherani, R. Zhu, Optoelectronic transport properties in ac silicon solar cell heterojunctions measured by frequency-domain photocarrier radiometry, Rev. Sci. Instrum. 86 (2015), 033901.
[19] T. Trupke, R.A. Bardos, M.C. Schubert, W. Warta, Photoluminescence imaging of silicon wafers, Appl. Phys. Lett. 89 (2006), 044107.
[20] J.A. Giesecke, M. The, M. Kasemann, W. Warta, Spatially resolved characterization of silicon as-cut wafers with photoluminescence imaging, Prog. Photovoltaics Res. Appl. 17 (2009) 217–225.
[21] T. Trupke, E. Pink, R.A. Bardos, M.D. Abbott, Spatially resolved series resistance of silicon solar cells obtained from luminescence imaging, Appl. Phys. Lett. 90 (2007), 093506.
[22] J.A. Giesecke, M.C. Schubert, B. Michl, F. Schindler, W. Warta, Minority carrier lifetime imaging of silicon wafers calibrated by quasi-steady-state photoluminescence, Sol. Energy Mater. Sol. Cells 95 (2011) 1011–1018.
[23] S.Y. Lim, S.P. Phang, T. Trupke, A. Cuevas, D. Macdonald, Dopant concentration imaging in crystalline silicon wafers by band-to-band photoluminescence, J. Appl. Phys. 110 (2011) 113712.
[24] J.Y. Liu, A. Melnikov, A. Mandelis, Silicon solar cell electrical parameter measurements through quantitative lock-in carrierographic (photoluminescence) and thermographic imaging, Phys. Status Solidi A 210 (2013) 2135–2145.
[25] F. Schindler, J. Giesecke, B. Michl, J. Schön, P. Krenckel, S. Riepe, W. Warta, M. C. Schubert, Material limits of multicrystalline silicon from state-of-the-art photoluminescence imaging techniques, Prog. Photovoltaics Res. Appl. 25 (2017) 499–508.
[26] Q.M. Sun, A. Melnikov, A. Mandelis, R.H. Pagliaro, Surface recombination velocity imaging of wet-cleaned silicon wafers using quantitative heterodyne lock-in carrierography, Appl. Phys. Lett. 112 (2018), 012105.
[27] P. Song, A. Melnikov, Q.M. Sun, A. Mandelis, J.Y. Liu, Contactless non-destructive imaging of doping density and electrical resistivity of semiconductor Si wafers using lock-in carrierography, Semicond. Sci. Technol. 33 (2018) 12LT01.
[28] L.L. Hu, A. Mandelis, Q.M. Sun, Ultrahigh-frequency heterodyne lock-in carrierography for large-scale quantitative multi-parameter imaging of colloidal quantum dot solar cells, IEEE J. Photovolt. 9 (2019) 132–138.
[29] J. Tolev, A. Mandelis, M. Pawlak, Nonlinear dependence of photocarrier radiometry signals from p-Si wafers on optical excitation intensity, J. Electrochem. Soc. 154 (2007) H983–H994.
[30] Q.M. Sun, A. Melnikov, J. Wang, A. Mandelis, Simultaneous determination of effective carrier lifetime and resistivity of Si wafers using the nonlinear nature of photocarrier radiometric signals, J. Phys. D Appl. Phys. 51 (2018) 15LT01.
[31] Q.M. Sun, A. Melnikov, A. Mandelis, Camera-based high frequency heterodyne lock-in carrierographic (frequency-domain photoluminescence) imaging of crystalline silicon wafers, Phys. Status Solidi A 213 (2016) 405–411.
[32] X.K. Lei, B.C. Li, Q.M. Sun, J. Wang, C.M. Gao, Nonlinear two-layer model for photocarrier radiometry of ion-implanted silicon wafers, AIP Adv. 9 (2019), 035125.
[33] X.K. Lei, B.C. Li, Q.M. Sun, J. Wang, C.M. Gao, Influence of nonlinearity on electronic transport characterization of ion-implanted silicon wafers, Int. J. Thermophys. 41 (2020) 3.
[34] X.K. Lei, B.C. Li, Q.M. Sun, J. Wang, C.M. Gao, Electronic transport characterization of B^+ ion-implanted silicon wafers with nonlinear photocarrier radiometry, J. Appl. Phys. 127 (2020), 035701.
[35] P. Würfel, Physics of Solar Cells: from Basic Principles to Advanced Concepts, Wiley-VCH, Weinheim, 2005.
[36] D.K. Schroder, Carrier lifetimes in silicon, IEEE Trans. Electron. Dev. 44 (1997) 160–170.
[37] R. Brendel, Note on the interpretation of injection-level-dependent surface recombination velocities, Appl. Phys. A 60 (1995) 523–524.
[38] J. Schmidt, Measurement of differential and actual recombination parameters on crystalline silicon wafers, IEEE Trans. Electron. Dev. 46 (1999) 2018–2025.
[39] R.A. Sinton, T. Trupke, Limitations on dynamic excess carrier lifetime calibration methods, Prog. Photovoltaics Res. Appl. 20 (2012) 246–249.
[40] J.A. Giesecke, W. Warta, Understanding carrier lifetime measurements at nonuniform recombination, Appl. Phys. Lett. 104 (2014), 082103.
[41] P. Song, A. Melnikov, Q.M. Sun, R.H. Pagliaro, X.G. Sun, J.Y. Liu, A. Mandelis, Surface recombination velocity on wet-cleaned silicon wafers using heterodyne lock-in carrierography imaging measurement uniqueness investigation, Semicond. Sci. Technol. 35 (2020), 055013.
[42] A. Mandelis, Diffusion-Wave Fields: Mathematical Methods and Green Functions, Springer, 2001.
[43] W.V. Roosbroeck, W. Shockley, Photon-radiative recombination of electrons and holes in germanium, Phys. Rev. 94 (1954) 1558–1560.
[44] A. Richter, S.W. Glunz, F. Werner, J. Schmidt, A. Cuevas, Improved quantitative description of auger recombination in crystalline silicon, Phys. Rev. B 86 (2012) 165202.
[45] W. Gerlach, H. Schlangenotto, H. Maeder, On the radiative recombination rate in silicon, Phys. Status Solidi A 13 (1972) 277–283.
[46] T. Trupke, M.A. Green, P. Wurfel, P.P. Altermatt, A. Wang, J. Zhao, R. Corkish, Temperature dependence of the radiative recombination coefficient of intrinsic crystalline silicon, J. Appl. Phys. 94 (2003) 4930–4937.
[47] J. Dziewior, W. Schmid, Auger coefficients for highly doped and highly excited silicon, Appl. Phys. Lett. 31 (1977) 346–348.
[48] A. Hangleiter, R. Hacker, Enhancement of band-to-band Auger recombination by electron-hole correlations, Phys. Rev. Lett. 65 (1990) 215–218.